

# Preparation and coherent manipulation of pure quantum states of a single molecular ion

Chin-wen Chou<sup>1</sup>, Christoph Kurz<sup>1</sup>, David B. Hume<sup>1</sup>, Philipp N. Plessow<sup>2</sup>, David R. Leibbrandt<sup>1,3</sup> & Dietrich Leibfried<sup>1</sup>

Laser cooling and trapping of atoms and atomic ions has led to advances including the observation of exotic phases of matter<sup>1,2</sup>, the development of precision sensors<sup>3</sup> and state-of-the-art atomic clocks<sup>4</sup>. The same level of control in molecules could also lead to important developments such as controlled chemical reactions and sensitive probes of fundamental theories<sup>5</sup>, but the vibrational and rotational degrees of freedom in molecules pose a challenge for controlling their quantum mechanical states. Here we use quantum-logic spectroscopy<sup>6</sup>, which maps quantum information between two ion species, to prepare and non-destructively detect quantum mechanical states in molecular ions<sup>7</sup>. We develop a general technique for optical pumping and preparation of the molecule into a pure initial state. This enables us to observe high-resolution spectra in a single ion (CaH<sup>+</sup>) and coherent phenomena such as Rabi flopping and Ramsey fringes. The protocol requires a single, far-off-resonant laser that is not specific to the molecule, so many other molecular ions, including polyatomic species, could be treated using the same methods in the same apparatus by changing the molecular source. Combined with the long interrogation times afforded by ion traps, a broad range of molecular ions could be studied with unprecedented control and precision. Our technique thus represents a critical step towards applications such as precision molecular spectroscopy, stringent tests of fundamental physics, quantum computing and precision control of molecular dynamics<sup>8</sup>.

Substantial progress has been made in recent years towards the goals of controlling the quantum mechanical states of ultracold molecules<sup>9,10</sup> (see also Methods). The charge of a molecular ion provides a means of trapping and sympathetically cooling translational motion via its Coulomb interaction with a co-trapped atomic ion that is readily laser-cooled<sup>11</sup>. Cooling of vibrational<sup>12</sup> and rotational<sup>13–16</sup> states has been realized in heteronuclear molecular ions. Preparation of molecules in specific vibrational and rotational states has been achieved via threshold photoionization<sup>17</sup>, and optical pumping into individual hyperfine states has been demonstrated<sup>18</sup>. In the context of quantum-logic spectroscopy, state detection of a single molecular ion in a particular subset of states in a rotational manifold has been achieved<sup>7</sup>. Many of these experiments rely on fortuitous molecular properties<sup>9,13</sup>, dedicated multi-laser systems<sup>9,14,15,18</sup> or sophisticated laser-cooling techniques<sup>10</sup>. Coherent control of pure quantum states of a molecular ion, which is crucial to precision experiments, has not yet been accomplished.

Here we demonstrate a general protocol for coherent manipulation of trapped molecular ions in their electronic and vibrational ground states based on quantum-logic spectroscopy<sup>6</sup> and stimulated Raman transitions driven by a far-detuned laser source<sup>19–21</sup>. Because the rotational motion is not cooled, our approach relies on probabilistically preparing a particular rotational state via a projective measurement<sup>22</sup>. We cool the shared motion of the molecular ion and a co-trapped atomic ion to the ground state<sup>11</sup>. We then set the relative detuning of the Raman beams to drive a specific transition in the molecule in such a way that a state change of the molecule is accompanied by an excitation of the shared

motion (motional sideband). We can efficiently detect this excitation with the atomic ion, which projects the molecule into the final state of the transition, leaving the molecule in a known, pure quantum state<sup>22</sup>. This method enables subsequent manipulation of the molecular state and spectroscopy of molecular transitions. In addition, we pump the molecular ion into specific sublevels of its rotational states, effectively orienting the molecular rotation along an axis of our choice. The improved orientation after pumping increases the success rate of state preparation and the signal-to-noise ratio in subsequent experiments.

In our experiments, we trap two <sup>40</sup>Ca<sup>+</sup> ions in a harmonic ion trap in ultra-high vacuum at room temperature (pressure  $\approx 4 \times 10^{-9}$  Pa). To form the molecular ion, hydrogen gas is leaked into the vacuum chamber until one of the <sup>40</sup>Ca<sup>+</sup> ions reacts to form a <sup>40</sup>CaH<sup>+</sup> ion, which quickly relaxes to its singlet electronic and vibrational ground state, but remains in a mixture of rotational states, in equilibrium with the black-body radiation of its room-temperature environment<sup>23</sup>. The <sup>40</sup>CaH<sup>+</sup> molecular ion serves as a test case for a much wider class of molecules that could be generated using various other techniques (see Methods). The <sup>40</sup>Ca<sup>+</sup> ion, which can readily be laser cooled, optically pumped and manipulated<sup>24</sup>, is coupled to the molecule by mutual Coulomb repulsion so that the shared normal modes of translational motion can be sympathetically cooled to their ground states<sup>7,11</sup>. A simplified diagram of the experimental set-up is shown in Fig. 1.

Rotation of the molecule and coupling of the rotational angular momentum  $\hat{J}$ , the spin of the proton  $\hat{I}$  and the external magnetic field  $\mathbf{B}$ , is described by the Hamiltonian

$$\hat{H}_{\text{rot}} = \frac{1}{\hbar}(2\pi R\hat{J}^2 - g\mu_{\text{N}}\hat{J} \cdot \mathbf{B} - g_I\mu_{\text{N}}\hat{I} \cdot \mathbf{B} - 2\pi c_{IJ}\hat{I} \cdot \hat{J}) \quad (1)$$

where  $R \approx 144$  GHz is the rotational constant for <sup>40</sup>CaH<sup>+</sup> (ref. 25),  $\mu_{\text{N}}$  is the nuclear magneton,  $g$  and  $g_I$  are the  $g$ -factors,  $c_{IJ}$  is the spin-rotation constant and  $\hbar = h/(2\pi)$  is the reduced Planck constant (see Methods). With  $|\mathbf{B}| \approx 0.36$  mT, we calculate energy levels of the eigenstates of  $\hat{H}_{\text{rot}}$ . Those for rotational quantum number  $J \in \{1, 2\}$  are displayed in Fig. 2. We classify the eigenstates by  $|\mathcal{J}\rangle \equiv |J, m, \xi\rangle$ , where  $\mathcal{J}$  is the set of quantum numbers  $\{J, m, \xi\}$ , in which  $J$  can be 0 or a positive integer and  $m \in \{-J-1/2, -J+1/2, J-1/2, J+1/2\}$  denotes the sum  $m = m_J + m_I$  of the components of the rotational angular momentum and the proton spin along  $\mathbf{B}$ . The value of  $m$  is a good quantum number (that is, it can be used to label energy eigenstates) for arbitrary  $\mathbf{B}$ . The label  $\xi \in \{+, -\}$  indicates the relative sign in the superposition of product states with the same  $m$  but opposite proton spin,  $|J, m_J = m + 1/2\rangle |m_I = -1/2\rangle$  and  $|J, m_J = m - 1/2\rangle |m_I = +1/2\rangle$  (see Methods). In the extreme states in which spin and rotational angular momentum are aligned with the quantization axis, the eigenstates are simple product states  $|J, \pm(J+1/2), \pm\rangle = |J, m_J = \pm J\rangle |m_I = \pm 1/2\rangle$  and the label  $\xi$  denotes the sign of  $\pm(J+1/2)$ . We operate at an intermediate magnetic field, at which the last three coupling terms in equation (1) lead to energy shifts of similar magnitude.

<sup>1</sup>Time and Frequency Division, National Institute of Standards and Technology, Boulder, Colorado 80305, USA. <sup>2</sup>Institute of Catalysis Research and Technology, Karlsruhe Institute of Technology, Karlsruhe, Germany. <sup>3</sup>University of Colorado, Boulder, Colorado, USA.

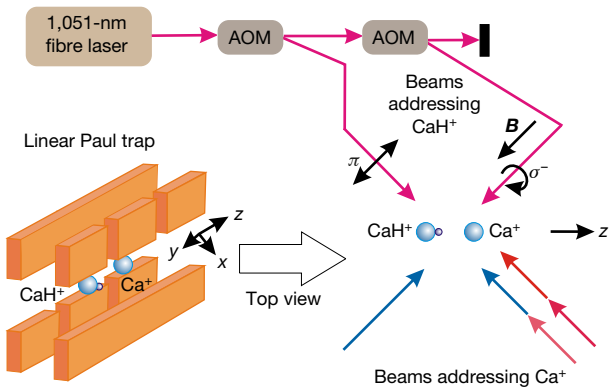


**Figure 1 | Simplified experimental set-up.** A  $^{40}\text{CaH}^+$ - $^{40}\text{Ca}^+$  ion pair is held in a linear Paul trap. Two modes of motion in the  $z$  direction and one in the  $x$  direction of the ion pair are prepared in the motional ground states via laser cooling on  $^{40}\text{Ca}^+$ . The motional mode in the  $z$  direction in which the two ions oscillate out of phase is used as the normal mode for the quantum-logic spectroscopy protocol. Two Raman beams derived from a single 1,051-nm fibre laser are split in frequency by two acousto-optic modulators (AOMs). They are directed onto the molecular ion with a  $k$ -vector difference along the trap  $z$  axis. The two Raman beams have  $\pi$  and  $\sigma^-$  polarizations relative to the quantization axis defined by the applied magnetic field  $B$ . They drive either carrier two-photon stimulated Raman transitions in the molecule or their motional sidebands, depending on the frequency detuning, while changing the projection quantum number  $m$  of the molecular angular momentum by  $\pm 1$ . Single quanta of excitation in the ion motion can be detected by driving sidebands of the narrow quadrupole transition between the  $4s^2S_{1/2}$  and  $3d^2D_{5/2}$  levels of the  $^{40}\text{Ca}^+$  atomic ion, followed by electron shelving detection with the laser beams addressing  $^{40}\text{Ca}^+$  (blue, red and pink arrows; see text and Methods). Detection of motional excitation on the  $^{40}\text{Ca}^+$  ion projects the molecule into the final state of the addressed transition, which is then available for further manipulation.

To drive the stimulated Raman transitions in the molecule, we use two Raman beams from a continuous-wave fibre laser with a wavelength of approximately 1,051 nm. The two beams are directed separately onto the ions, one circularly ( $\sigma^-$ ) and one linearly ( $\pi$ ) polarized with respect to the quantization axis along the magnetic field, as indicated in Fig. 1. With  $\Delta\nu \equiv \nu_\sigma - \nu_\pi$  tuned near  $\pm(E_f - E_i)/h$  and  $\pm[(E_f - E_i)/h \pm \nu_i]$ , these beams coherently drive carrier two-photon stimulated Raman transitions and the first sidebands of translational motion, respectively. Here  $\nu_\sigma$  ( $\nu_\pi$ ) is the frequency of the  $\sigma^-$ -polarized ( $\pi$ -polarized) beam,  $E_i$  ( $E_f$ ) is the energy of the initial (final) molecular level and  $\nu_i$  is the frequency of the motional mode. To minimize the perturbation of the molecular energy levels that is caused by the Raman beams, we control the intensity ratio between the  $\sigma^-$  and  $\pi$  beams to minimize the differential AC Stark shifts between the molecular levels (see Methods).

Within the framework of quantum-logic spectroscopy, the probabilistic projective preparation of a pure quantum state in the molecular ion proceeds as follows. If we assume perfect ground-state cooling, with  $^{40}\text{Ca}^+$  prepared in  $|D\rangle \equiv |D_{5/2}, m = -5/2\rangle$ , then the density matrix of the molecule, the normal mode, and the atomic ion can be written as

$$\rho_0 = \left( \sum_{\mathcal{J}} P_{\mathcal{J}} |\mathcal{J}\rangle \langle \mathcal{J}| \right) |n=0\rangle \langle n=0| |D\rangle \langle D|$$

where  $P_{\mathcal{J}}$  is the population in state  $|\mathcal{J}\rangle$ , and  $|n\rangle$  denotes the motional state with  $n \in \{0, 1, 2, \dots\}$  phonons in the normal mode. With probability  $P_{\mathcal{J}}$ , the molecule is in state  $|\mathcal{J}_i\rangle$  and we can drive the molecular blue-sideband transition  $|\mathcal{J}_i\rangle|0\rangle|D\rangle \rightarrow (\alpha|\mathcal{J}_i\rangle|0\rangle + \beta|\mathcal{J}_f\rangle|1\rangle)|D\rangle$ , with  $|\alpha|^2 + |\beta|^2 = 1$  and selection rule  $m_f = m_i \pm 1$ . If the  $|\mathcal{J}_i\rangle \leftrightarrow |\mathcal{J}_f\rangle$

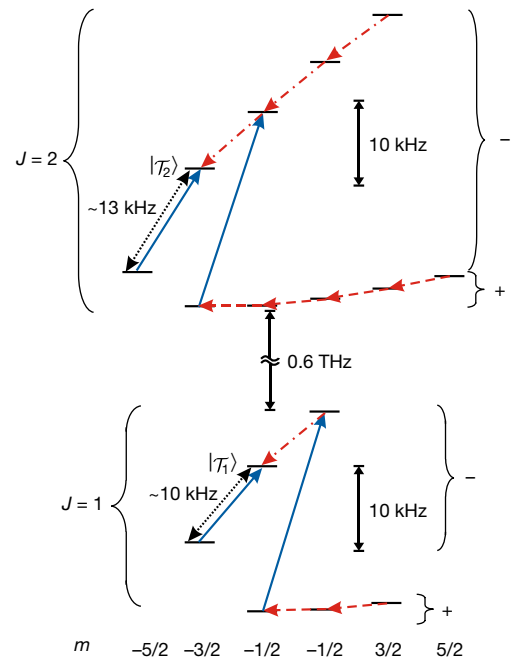


**Figure 2 | Level diagrams for the rotational levels of  $^{40}\text{CaH}^+$  for  $J \in \{1, 2\}$ .** At  $|B| \approx 0.36$  mT, the energy eigenstates  $|J, m, \pm\rangle$  are either superpositions of product states of rotation and nuclear spin sublevels that add to the same total  $m$ , or extreme states in which the proton spin and the rotation are aligned ( $m = \pm(J + 1/2)$ ; see text and Methods). The red dashed, red dot-dashed and blue solid arrows indicate the directionality of the optical pumping transitions for population concentration. Red dashed and dot-dashed arrows indicate that several transitions can be addressed simultaneously within the spectral resolution of the pumping sequence; blue arrows indicate transitions with resolved frequencies. The black dotted arrows show the  $|\mathcal{T}_i\rangle = |J, -J + 1/2, -\rangle \leftrightarrow |J, -J - 1/2, -\rangle$  target transitions with unique frequencies that are driven for the projective pure state preparation and coherent manipulation (see text).

transition has a unique frequency in the molecule, then the density matrix of the system is modified to

$$\rho_1 = P_{\mathcal{J}_i} (\alpha|\mathcal{J}_i\rangle|0\rangle + \beta|\mathcal{J}_f\rangle|1\rangle) (\alpha^*\langle\mathcal{J}_i| \langle 0| + \beta^*\langle\mathcal{J}_f| \langle 1|) |D\rangle \langle D| + \left( \sum_{\mathcal{J} \neq \mathcal{J}_i} P_{\mathcal{J}} |\mathcal{J}\rangle \langle \mathcal{J}| \right) |0\rangle \langle 0| |D\rangle \langle D| \quad (2)$$

At this point we can attempt to drive a  $\pi$  pulse on the red sideband of  $^{40}\text{Ca}^+$ , which induces the transition  $|1\rangle|D\rangle \rightarrow |0\rangle|S\rangle$ , where  $|S\rangle$  denotes the  $S_{1/2}$ ,  $m = -1/2$  state of  $^{40}\text{Ca}^+$ . Fluorescence detection on  $^{40}\text{Ca}^+$  distinguishes the  $|S\rangle$  state, which scatters many photons, from the  $|D\rangle$  state, which ideally scatters no photons. High detection fidelity is achieved in a single shot by checking the resultant photon counts against a pre-determined threshold (see Methods and refs 26, 27). Therefore, with probability  $P_{\mathcal{J}_i} |\beta|^2$ , the density matrix of the molecule is projected to the pure state  $\rho_M = |\mathcal{J}_f\rangle \langle \mathcal{J}_f|$ , which is heralded non-destructively by detecting that the  $^{40}\text{Ca}^+$  ion scatters photons. We can measure Raman spectra of molecular transitions by recording the probability of detecting  $|S\rangle$ , as long as we leave the molecule enough time to re-establish equilibrium with the blackbody environment, so that  $P_{\mathcal{J}_i}$  is the same for every attempt. Such a spectrum with  $m_f = m_i - 1$  is shown as the blue curve in Fig. 3. Owing to the small magnitudes of  $P_{\mathcal{J}}$  ( $< 1.1\%$  at 300 K), the transitions with frequencies  $\omega/(2\pi) \equiv (E_f - E_i)/h$  between  $-10$  kHz and  $-50$  kHz are not discernible from measurement noise, which we have optimized to be at the 0.5% level (see Methods).

To achieve a better signal-to-noise ratio in the target transitions with unique frequencies ( $|J, -J + 1/2, -\rangle \leftrightarrow |J, -J - 1/2, -\rangle$ ), it is beneficial to increase the populations in the corresponding initial states above

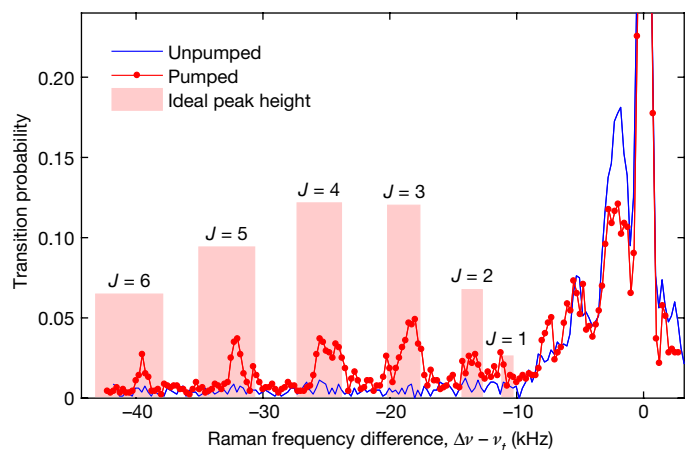


**Figure 3 | Raman spectra for  $\Delta m = -1$  blue-sideband transitions probed with 1-ms pulses.** The frequency axis shows the offset from the motional frequency ( $\nu_i \approx 5.164$  MHz) of the normal mode. Data without optical pumping (blue line) show two prominent peaks, near  $-2$  kHz and  $-6$  kHz, that correspond to the transitions  $|J, m, \xi\rangle \rightarrow |J, m-1, \xi\rangle$  (which overlap for different  $m$ ) for the two cases  $\xi \in \{+, -\}$  shown by the red dashed and dot-dashed arrows, respectively, in Fig. 2. Peaks between  $0$  kHz and  $-10$  kHz are visible because they arise from a large number of sublevels. The peak at  $0$  kHz is attributed to coherent motion that can be driven by modulated optical dipole forces without changing the internal state of the molecule if the polarization of the Raman beams is not perfectly orthogonal on both ions. Data with optical pumping (red dots) show peaks near  $\{-11, -14, -19, -25, -32, -40\}$  kHz, which are identified as the  $|J, -J+1/2, -\rangle \rightarrow |J, -J-1/2, -\rangle$  transitions for  $J \in \{1, 2, 3, 4, 5, 6\}$ , respectively, from their proximity to the predicted frequencies (see Methods). Pink-shaded bars indicate the frequencies and heights of the peaks predicted by theory, with the effect of  $J$ -dependent Rabi rates taken into account. The widths of the bars indicate the ranges of the predicted transition frequencies (see Methods).

the thermal equilibrium levels. Because the blackbody relaxation times (about  $100$  ms to more than  $2$  s at  $300$  K for  $J < 8$ ) are long compared with attempts to drive transitions ( $< 5$  ms), we can concentrate the

population via optical pumping. The pumping uses a pulse sequence similar to projective state preparation. The ions are first cooled to the ground state of motion, after which a blue-sideband pulse is applied to the molecular transition to be pumped. Further ground-state cooling produces dissipation in the system, making these pumping transitions directional<sup>6</sup>, analogous to a typical optical pumping process in which spontaneous decay removes entropy from the system. The effect of pumping in the molecular system can be understood by returning to equation (2), which describes the density matrix of the system after the blue-sideband pumping pulse on the molecular ion. In this case,  $J_i$  denotes the state being pumped. If  $|\beta| \neq 0$  after the pumping attempt, then the sideband cooling pulses on the  $^{40}\text{Ca}^+$  ion destroy the coherence induced from driving the molecular blue-sideband transition, transforming the density matrix from  $\rho_1$  to

$$\rho_2 = \left[ P_{\mathcal{J}_i} |\alpha|^2 |\mathcal{J}_i\rangle\langle\mathcal{J}_i| + (P_{\mathcal{J}_i} |\beta|^2 + P_{\mathcal{J}_f}) |\mathcal{J}_f\rangle\langle\mathcal{J}_f| + \sum_{J \neq \mathcal{J}_i, \mathcal{J}_f} P_J |\mathcal{J}\rangle\langle\mathcal{J}| \right] |0\rangle\langle 0| |D\rangle\langle D|$$

The population of  $|\mathcal{J}_i\rangle$  is decreased to  $P_{\mathcal{J}_i} |\alpha|^2$  while the population of  $|\mathcal{J}_f\rangle$  is increased to  $P_{\mathcal{J}_f} + P_{\mathcal{J}_i} |\beta|^2$ . When repeating this sequence on the transitions indicated by the blue solid, red dashed and red dot-dashed arrows in Fig. 2, the directionality of the transfer of angular momentum pumps the population towards the target states, which for each  $J \in \{1, 2, 3, \dots\}$  are denoted by the set of quantum numbers  $\mathcal{T}_J = \{J, m = -J + 1/2, -\}$ . We could pump to a different subset of states by modifying the choice of transitions and their directionality. The quantization axis and beam polarizations can be chosen to orient the rotational axis and the proton spin of the resultant pumped molecular state as desired.

For  $^{40}\text{CaH}^+$  in  $|\mathbf{B}| = 0.36$  mT, the frequencies of the transitions  $|J, m, +\rangle \rightarrow |J, m-1, +\rangle$  and  $|J, m, -\rangle \rightarrow |J, m-1, -\rangle$ , indicated by the red dashed and dot-dashed arrows in Fig. 2, are in two narrow regions around  $-2$  kHz and  $-6$  kHz, respectively (see Figs 2 and 3); consequently, multiple transitions can be pumped simultaneously. To pump the majority of the population to the target states, transitions

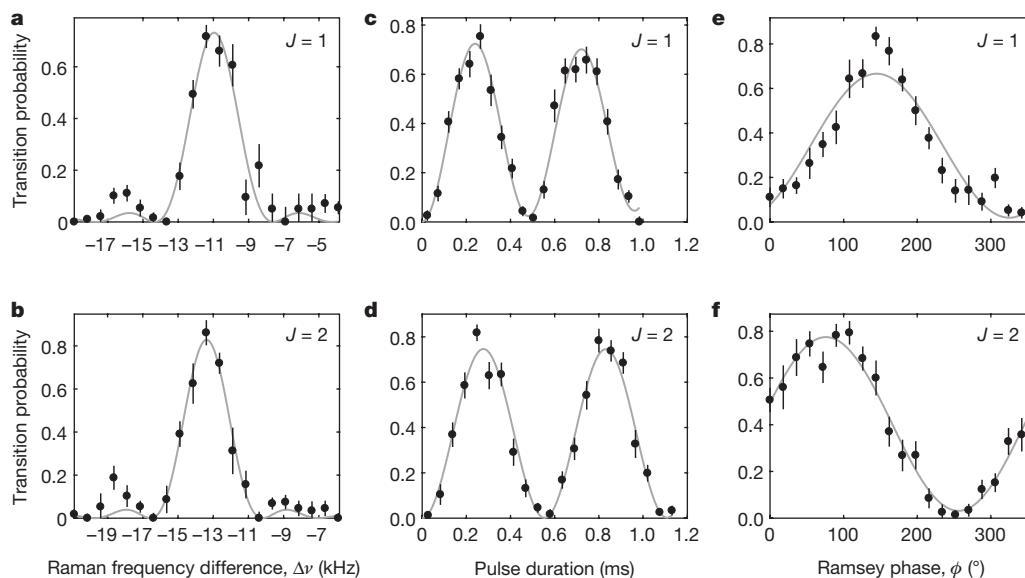


**Figure 4 | Coherent spectroscopy and manipulation of pure molecular states.** The  $|J, -J-1/2, -\rangle$  state with  $J=1$  (a, c, e) or  $J=2$  (b, d, f) is prepared using adaptive molecular state preparation, followed by interrogation of the  $|J, -J-1/2, -\rangle \leftrightarrow |T_J\rangle = |J, -J+1/2, -\rangle$  transition. a, b, Frequency spectra; c, d, Rabi flopping. The grey lines in a and b (c and d) are fits to  $\text{sinc}^2(x) = [\sin(x)/x]^2$  functions

(exponentially damped sinusoids). e, f, Ramsey fringes as a function of the relative phase  $\phi$  between the two  $\pi/2$  pulses with a wait time of  $15$  ms. The grey lines are fits to sinusoidal functions with periods of  $360^\circ$ . All error bars,  $\pm$ s.d. Data acquisition time, approximately  $30$  min (a, b),  $1$  h (c, d) or  $45$  min (e, f).

with  $\omega/(2\pi) > 10$  kHz (blue solid arrows in Fig. 2) also need to be addressed with additional pumping pulses. Assuming perfect pumping efficiency, the steady-state density matrix can be approximated by

$$\rho_p = \left( \frac{1}{2} Q_0 \sum_{J=0} |\mathcal{T}_J\rangle\langle\mathcal{T}_J| + \sum_{J>0} Q_J \left| J, -J + \frac{1}{2}, - \right\rangle \left\langle J, -J + \frac{1}{2}, - \right| \right) |0\rangle\langle 0| |D\rangle\langle D|$$

where  $Q_J = \sum_{m,\xi} P_{J,m,\xi}$  is the total probability of being in the manifold with rotational quantum number  $J$ , which, compared to the equilibrium thermal distribution, increases the probability of being in  $|J, -J + 1/2, - \rangle$  by a factor of  $2(2J + 1)$  (the number of sublevels in the manifold). The Raman spectrum taken after the pumping stage is shown as the linked red dots in Fig. 3. The excitation probabilities for the isolated target transitions are much greater than those for the equilibrium spectrum, but we infer a pumping efficiency of less than 50%.

After optical pumping, the frequencies of the target transitions are distinguishable and enable projective state preparation. False-positive detection of changes in phonon number can be due to imperfect ground-state cooling or heating of the motion from other sources, which affects the fidelity of the projective state preparation. We can improve the preparation fidelity by performing multiple projective measurements that successively drive the  $|\mathcal{T}_J\rangle|0\rangle \leftrightarrow |J, -J - 1/2, - \rangle|1\rangle$  transition with  $\pi$  pulses. Repeated detection of the changes in phonon number increases the preparation fidelity of the desired state to approximately 80% (see Methods).

After state preparation, the resultant quantum state can be coherently manipulated. We observe Rabi flopping of the molecule by driving the carrier transition  $|J, -J - 1/2, - \rangle \leftrightarrow |\mathcal{T}_J\rangle$  for different durations and detecting changes in the molecular state by checking whether  $\pi$  pulses on the sideband transition  $|\mathcal{T}_J\rangle|0\rangle \leftrightarrow |J, -J - 1/2, - \rangle|1\rangle$  alter the motional state. To avoid driving multiple transitions, the carrier Raman pulses are reduced in power by a factor of 10 compared to the sideband pulses. During the coherent evolution, the state of the molecule is ideally

$$|\Psi(t)\rangle = \cos(\Omega_J t) \left| J, -J - \frac{1}{2}, - \right\rangle + \sin(\Omega_J t) |\mathcal{T}_J\rangle$$

where  $\Omega_J$  is the  $J$ -dependent Rabi frequency of the transition (see Methods). The molecule is detected in  $|\mathcal{T}_J\rangle$  with probability  $C_J \sin^2(\Omega_J t)$ , where  $C_J < 1$  because of inefficiencies in preparation and detection and imperfections in the driving pulse. By repeating preparation, coherent evolution and state detection, we build up sufficient statistics to observe the Rabi flops shown in Fig. 4 as a function of the duration of the Raman pulses for  $J \in \{1, 2\}$ .

To further characterize the coherence, we implement a Ramsey sequence. We first prepare an equally weighted superposition  $(|\mathcal{T}_J\rangle + |J, -J - 1/2, - \rangle)/\sqrt{2}$  by choosing  $\Delta\nu = -(E_f - E_i)/h$  and  $\Omega_J t = \pi/4$  to apply a carrier  $\pi/2$  pulse. We then wait for a duration  $T$  and apply another  $\pi/2$  pulse with variable phase  $\phi$  relative to the first pulse. If the molecular state remains coherent through the second interaction, then the probability to return to  $|\mathcal{T}_J\rangle$  varies sinusoidally with the relative phase. Fig. 4e, f shows this for  $J \in \{1, 2\}$  and  $T = 15$  ms. The fringes are suitable for metrology with sub-100-Hz resolution, although the systematic uncertainties have not yet been characterized at this level. The stability of the Raman beams could be further improved to better exploit the lifetime of the molecule in the rotational sublevels and achieve higher spectroscopic resolution with a longer Ramsey sequence.

The main criteria for applying the protocol demonstrated here to other molecular ion species are: (a) efficient trapping and sympathetic cooling via an atomic ion; and (b) transitions in the molecule with accessible frequencies and sufficient coherence for probabilistic

projective preparation and coherent manipulation of pure states (see Methods). The same laser and methods in our set-up are readily applicable to precision spectroscopy and quantum state manipulation of a wide range of molecular species, including symmetric molecules and possibly molecules that have been identified as candidates to impose stringent limits on the electric dipole moment of the electron<sup>28,29</sup>, or the time dependence of fundamental constants (see Methods and references therein). In future work, we plan to use a frequency comb as a second source of Raman pulses that can span the energy difference between rotational levels with different  $J$  (refs 19–21). Rather than relying on blackbody radiation to randomly populate a level with the desired  $J$ , this should allow us to coherently transfer the molecule from any pure state to the desired state on timescales much faster than the blackbody rates<sup>19–21</sup>. We are optimistic that these techniques will enable precise spectroscopic experiments on a multitude of molecular ions that are relevant in astrophysics, stringent tests of fundamental theories, and quantum information processing.

**Online Content** Methods, along with any additional Extended Data display items and Source Data, are available in the online version of the paper; references unique to these sections appear only in the online paper.

**Received 25 November 2016; accepted 20 March 2017.**

- Bloch, I., Dalibard, J. & Zwierger, W. Many-body physics with ultracold gases. *Rev. Mod. Phys.* **80**, 885–964 (2008).
- Mitchell, T. B. *et al.* Direct observations of structural phase transitions in planar crystallized ion plasmas. *Science* **282**, 1290–1293 (1998).
- Kitching, J., Knappe, S. & Donley, E. A. Atomic sensors—a review. *IEEE Sens. J.* **11**, 1749–1758 (2011).
- Ludlow, A. D., Boyd, M. M., Ye, J., Peik, E. & Schmidt, P. O. Optical atomic clocks. *Rev. Mod. Phys.* **87**, 637–701 (2015).
- Schiller, S. & Korobov, V. Tests of time independence of the electron and nuclear masses with ultracold molecules. *Phys. Rev. A* **71**, 032505 (2005).
- Schmidt, P. O. *et al.* Spectroscopy using quantum logic. *Science* **309**, 749–752 (2005).
- Wolf, F. *et al.* Non-destructive state detection for quantum logic spectroscopy of molecular ions. *Nature* **530**, 457–460 (2016).
- Carr, L. D., DeMille, D., Krems, R. V. & Ye, J. Cold and ultracold molecules: science, technology and applications. *New J. Phys.* **11**, 055049 (2009).
- Shuman, E. S., Barry, J. F. & Demille, D. Laser cooling of a diatomic molecule. *Nature* **467**, 820–823 (2010).
- Ospelkaus, S. *et al.* Controlling the hyperfine state of rovibronic ground-state polar molecules. *Phys. Rev. Lett.* **104**, 030402 (2010).
- Barrett, M. D. *et al.* Sympathetic cooling of  $^9\text{Be}^+$  and  $^{24}\text{Mg}^+$  for quantum logic. *Phys. Rev. A* **68**, 042302 (2003).
- Rellergert, W. G. *et al.* Evidence for sympathetic vibrational cooling of translationally cold molecules. *Nature* **495**, 490–494 (2013).
- Lien, C.-Y. *et al.* Broadband optical cooling of molecular rotors from room temperature to the ground state. *Nat. Commun.* **5**, 4783 (2014).
- Staanum, P. F., Højbjerg, K., Skyt, P. S., Hansen, A. K. & Drewsen, M. Rotational laser cooling of vibrationally and translationally cold molecular ions. *Nat. Phys.* **6**, 271–274 (2010).
- Schneider, T., Roth, B., Duncker, H., Ernsting, I. & Schiller, S. All-optical preparation of molecular ions in the rovibrational ground state. *Nat. Phys.* **6**, 275–278 (2010).
- Hansen, A. K. *et al.* Efficient rotational cooling of Coulomb-crystallized molecular ions by a helium buffer gas. *Nature* **508**, 76–79 (2014).
- Tong, X., Winney, A. H. & Willitsch, S. Sympathetic cooling of molecular ions in selected rotational and vibrational states produced by threshold photoionization. *Phys. Rev. Lett.* **105**, 143001 (2010).
- Bressel, U. *et al.* Manipulation of individual hyperfine states in cold trapped molecular ions and application to HD<sup>+</sup> frequency metrology. *Phys. Rev. Lett.* **108**, 183003 (2012).
- Schmidt, P. O. *et al.* Spectroscopy of atomic and molecular ions using quantum logic. *ALP Conf. Proc.* **862**, 305–312 (2006).
- Leibfried, D. Quantum state preparation and control of single molecular ions. *New J. Phys.* **14**, 023029 (2012).
- Ding, S. & Matsukevich, D. N. Quantum logic for the control and manipulation of molecular ions using a frequency comb. *New J. Phys.* **14**, 023028 (2012).
- Vogelius, I. S., Madsen, L. B. & Drewsen, M. Probabilistic state preparation of a single molecular ion by projection measurement. *J. Phys. B* **39**, S1259–S1265 (2006).
- Kimura, N. *et al.* Sympathetic crystallization of CaH<sup>+</sup> produced by a laser-induced reaction. *Phys. Rev. A* **83**, 033422 (2011).
- Roos, Ch. *et al.* Quantum state engineering on an optical transition and decoherence in a Paul trap. *Phys. Rev. Lett.* **83**, 4713–4716 (1999).

25. Abe, M., Moriwaki, Y., Hada, M. & Kajita, M. Ab initio study on potential energy curves of electronic ground and excited states of  $^{40}\text{CaH}^+$  molecule. *Chem. Phys. Lett.* **521**, 31–35 (2012).
26. Leibfried, D., Blatt, R., Monroe, C. & Wineland, D. Quantum dynamics of single trapped ions. *Rev. Mod. Phys.* **75**, 281–324 (2003).
27. Myerson, A. H. *et al.* High-fidelity readout of trapped-ion qubits. *Phys. Rev. Lett.* **100**, 200502 (2008).
28. Meyer, E. R., Bohn, J. L. & Deskevich, M. P. Candidate molecular ions for an electron electric dipole moment experiment. *Phys. Rev. A* **73**, 062108 (2006).
29. Loh, H. *et al.* Precision spectroscopy of polarized molecules in an ion trap. *Science* **342**, 1220–1222 (2013).

**Acknowledgements** We thank K. C. Cossel, Y. Wan and D. J. Wineland for comments on the manuscript. This work was supported by the US Army Research Office and the NIST quantum information programme. C.K. acknowledges support from the Alexander von Humboldt foundation. P.N.P.

acknowledges support by the state of Baden-Württemberg through bwHPC. This is a contribution of the National Institute of Standards and Technology, not subject to US copyright.

**Author Contributions** C.-w.C. and D.L. conceived and designed the experiments. C.-w.C. and C.K. developed components of the experimental apparatus, and collected and analysed data. C.-w.C. and D.L. wrote the manuscript. D.B.H. and D.R.L. contributed to the development of experimental methods and pulse sequences. P.N.P. computed the molecular constants and level structure. All authors provided suggestions for the experiments, discussed the results and contributed to editing the manuscript.

**Author Information** Reprints and permissions information is available at [www.nature.com/reprints](http://www.nature.com/reprints). The authors declare no competing financial interests. Readers are welcome to comment on the online version of the paper. Publisher's note: Springer Nature remains neutral with regard to jurisdictional claims in published maps and institutional affiliations. Correspondence and requests for materials should be addressed to C.-w.C. ([chin-wen.chou@nist.gov](mailto:chin-wen.chou@nist.gov)).

## METHODS

**Additional references.** The breakthroughs enabled by laser cooling and trapping of atoms and atomic ions in realizing exotic phases of matter are summarized in refs 2 and 30–33. Opportunities offered by precision experiments with cold trapped molecules have been explored<sup>18,34</sup> for precision metrology<sup>5,35,36</sup> and quantum information science<sup>37,38</sup>. In addition to coherent optical control<sup>10</sup>, coherent microwave control of ultracold molecules was recently demonstrated<sup>39</sup>. Some of the schemes proposed to reduce the number of states occupied by molecular ions can be found in refs 19, 22 and 40–43, with notable similarity between the scheme proposed in ref. 22 and that demonstrated here. Forming  $^{40}\text{CaH}^+$  via laser-induced reaction and sympathetic cooling of  $^{40}\text{CaH}^+$  with  $^{40}\text{Ca}^+$  ions was studied in ref. 23; ground-state cooling of a  $^{40}\text{CaH}^+ \cdot ^{40}\text{Ca}^+$  pair was reported in ref. 44.

**Generality of our approach and special applications.** Sympathetic cooling and quantum-logic readout require that the motion of the molecular ion and the logic ion are sufficiently coupled<sup>20</sup>. The amplitude of the heavier ion decreases and the frequency difference between the two normal modes increases as the mass ratio of the constituents becomes more unequal. An additional factor is that the radial pseudo-potential of linear radio-frequency traps scales with the inverse mass; therefore, the disparity in the radial frequencies also increases when masses become more different. Quantum-logic experiments have been done at mass ratios of up to three<sup>6</sup>, and this ratio could probably be pushed higher. Examples of well-characterized logic ions are  $^9\text{Be}^+$ ,  $^{25}\text{Mg}^+$ ,  $^{40}\text{Ca}^+$ ,  $^{88}\text{Sr}^+$ ,  $^{138}\text{Ba}^+$  and  $^{171}\text{Yb}^+$ . Use of these species should allow a range of diatomic and polyatomic molecules with masses from 3 a.m.u. to 513 a.m.u., sufficiently high to co-trap ions of small organic compounds. Despite the fact that their mass ratio is larger than three, we are optimistic that the lightest molecular ion,  $\text{H}_2^+$  (refs 45–47), can be made accessible using  $^9\text{Be}^+$  as the logic ion<sup>48</sup>.

The single continuous-wave laser at 1,051 nm used here, or similar continuous-wave sources, can address Raman transitions between states with energy differences ranging from a few hundred hertz to tens of gigahertz, provided that the two Raman beams can be separated in frequency with suitable acousto-optic or electro-optic devices, as demonstrated here. In this way, the energy levels split by a few to several tens of kilohertz that arise from the coupling of nuclear magnetic moments to those induced by molecular rotation, and from coupling of such magnetic moments to weak external magnetic fields similar to the states used here, can be addressed. Energy splittings due to coupling of the electron spins with the rotation, hyperfine and Zeeman structure, which typically range from a few megahertz to 10 GHz, can also be bridged in this manner.

Stimulated Raman transitions with reasonable Rabi frequencies are feasible in symmetric molecules, despite their lack of a permanent dipole moment. This is also true for  $\text{H}_2^+$ , which has no stable excited electronic state. With sufficiently high detuning, the population in excited states can be kept small enough that the probability of dissociation becomes negligible. Nevertheless, the electric fields due to the Raman beams deform the electronic ground state in such a way that it has a polarization component at energy differences that arise within the electronic ground-state manifold as a result of vibration, rotation, hyperfine structure and so on. Owing to its unbound excited electronic state, the sum over excited states that we evaluate below cannot be used for computing the Raman–Rabi frequency in  $\text{H}_2^+$ . However, the Rabi frequency can be computed using other methods<sup>47</sup>. For light with a wavelength of around 800 nm, 750 mW per Raman beam and focused to a  $20\text{-}\mu\text{m}^2$  waist, the Rabi frequency is estimated to be  $2\pi \times 29\text{ kHz}$  for a carrier transition (L. Hilico & J.-Ph. Karr, private communication).

The search for an electron electric dipole moment could be realized by combining our methods with those described in ref. 29. This experiment uses a linear trap with extra electrodes to superimpose a rotating radial electric field onto the trapping fields. If the radial electric field rotation frequency is much faster than the radial secular frequency of the ions, then it leads to additional circular micro-motion at the frequency of the rotating field. The micro-motion excursions of the ions are essentially  $180^\circ$  out of phase with the rotating electric field, so they experience a field of constant magnitude, but with a zero average over one rotation period. Owing to couplings between the electron spin and the molecular rotation, the lowest energy splittings (due to  $\Lambda$  doubling<sup>29</sup>) that dictate adiabaticity are around 10 MHz. In the experiments described in ref. 29, the field has a magnitude of  $11.6\text{ V cm}^{-1}$  and rotates at 253 kHz. In a linear trap with 2-mm distances between opposing electrodes, such a rotating field could be achieved with less than 3 V of amplitude, considerably below the amplitudes that are commonly used for producing the radial confinement in linear traps of such dimensions (tens to hundreds of volts). However, the extent of the circular motion of the ions will be sizable (about  $200\text{ }\mu\text{m}$ ) and the secular frequencies will be limited to tens of kilohertz. Quantum-logic spectroscopy at such low secular frequencies has not yet been demonstrated. The rotating field does not need to be turned on during the quantum-logic interrogation. If all technical obstacles can be overcome, then

the question still remains whether experiments of a single or few molecular ions will offer an advantage over the larger ensembles that are currently probed in the experiments described in ref. 29. For that, the advantage of large ion number needs to be overcompensated by an increased coherence time and precision. It seems conceivable that this could be the case, because the coherence time demonstrated in ref. 29 was probably limited by uncontrolled ion–ion interactions. Moreover, the quantum-logic set-up may allow different molecular ions to be co-trapped with the logic ion simultaneously and hence to be non-destructively probed in the same environment. This set-up might be advantageous to further suppress systematic uncertainties.

Another field of current interest is to use molecular transitions to increase the sensitivity of searches for the variation of fundamental constants. Vibrational transitions are most sensitive to variations in the ratio of electron to proton mass  $m_e/m_p$  and probing them will require dedicated lasers. Nevertheless, the methods demonstrated here enable efficient state preparation and non-destructive state read-out with near-unity quantum efficiency, and thereby overcome major hurdles on the way to such experiments. The species used in our experiments,  $\text{CaH}^+$ , has been identified as a candidate for testing the time dependence of  $m_e/m_p$ , as have other Earth-alkali halides ( $\text{SrH}^+$ ,  $\text{YbH}^+$ )<sup>49</sup> and  $\text{NH}^+$  (ref. 50) that have a similar level structure. Manipulation of  $\text{H}_2^+$  and  $\text{HD}^+$  (ref. 5) is discussed in more detail above.

The symmetric molecules  $\text{N}_2^+$  (ref. 51) and  $\text{O}_2^+$  (ref. 52) have also been suggested as viable candidates, with little coupling to the environment due to the lack of a permanent dipole moment. Both are a good match for  $\text{Ca}^+$  as the logic ion and have magnetic dipole moments that allow them to be projected and measured with a continuous-wave source and suitable acousto-optic or electro-optic devices, as described above. The species discussed in ref. 53 ( $\text{HBr}^+$ ,  $\text{HI}^+$ ,  $\text{Br}_2^+$ ,  $\text{I}_2^+$ ,  $\text{IBr}^+$ ,  $\text{ICl}^+$  and  $\text{IF}^+$ ) all have a  $\Pi$  electronic ground state that leads to a magnetic moment due to the orbital angular momentum of the electrons that will provide accessible transitions, with more level splittings provided by additional magnetic moments. However, these ions are heavier, so  $\text{Ba}^+$  or  $\text{Yb}^+$  might be a more suitable logic ion.

**Numerical calculation of  $\text{CaH}^+$  properties.** Calculating the properties of  $\text{CaH}^+$  requires an accurate potential energy curve to determine the equilibrium structure and rovibrational wavefunctions within the Born–Oppenheimer approximation. In a second step, properties (spin-rotation constant and  $g$ -factor) are computed as a function of the Ca–H internuclear distance  $r$ . The  $g$ -factor and spin-rotation constant for a given rovibrational state  $|Jv\rangle$  are computed as the expectation value with respect to the rovibrational wavefunction; for example,  $g_J = \langle \Psi_J(r) | g(r) | \Psi_J(r) \rangle$ . **Geometry and vibrational wavefunction of  $\text{CaH}^+$ .** Calculations were carried out using the packages CFOUR<sup>54</sup> and MRCC<sup>55,56</sup> using coupled-cluster (CC) methods. Different levels of coupled-cluster theory are abbreviated according to the level of excitations in the exponential; for example, CCSDTQ stands for coupled-cluster with single, double, triple and quadruple excitations. In CCSD(T), the contribution of triple excitations is determined from perturbation theory<sup>57</sup>. All calculations use atom-centred Gaussian basis sets, the correlation-consistent polarized (cc-p) basis sets<sup>58,59</sup>, with valence-only (cc-pV) and core–valence (cc-pCV) correlation for Ca. The full basis set is specified by the number  $X$  of independent radial basis functions per correlated occupied orbital, for example cc-pCV5Z. All calculations are based on a closed-shell restricted Hartree–Fock reference. The frozen-core approximation was used in coupled-cluster calculations, with the five lowest (doubly occupied) orbitals in the frozen core. In the following, we are not interested in total energies, but only in the shape of the potential-energy curve. As can be seen in Extended Data Fig. 1, the energy is well converged with respect to the cluster operator at the CCSDT level of theory. This follows from comparison with CCSDTQ calculations, with deviations of less than 0.01 eV. In the range of the potential curve that is relevant for the vibrational ground state (approximately  $1.4\text{ \AA} < r < 2.4\text{ \AA}$ ; see Extended Data Figs 2 and 3), CCSD(T) agrees quantitatively with CCSDT. For  $r > 3.0\text{ \AA}$ , CCSD(T) starts to deviate substantially from CCSDT because the calculation of the amplitudes of the triple excitations from perturbation theory is no longer a good approximation of the solution of the coupled-cluster equations. We therefore use CCSD(T) because it is accurate enough and the most efficient. Increasing the basis set from cc-pCVQZ to cc-pCV5Z results in energy changes of less than 0.02 eV. The contribution of the diagonal Born–Oppenheimer correction and of scalar relativistic effects, mass–velocity correction and one-electron Darwin term corrections are also about 0.02 eV.

Vibrational wavefunctions are obtained by numerical solution of the Schrödinger equation using the full potential  $V_0(r)$  (energy of the electronic wavefunction as a function of Ca–H distance, using CCSD(T)) plus centrifugal potential:

$$V(r) = V_0(r) + \frac{\hbar^2 J(J+1)}{2\mu r^2}$$

where  $\mu$  is the reduced mass and  $J$  is the rotational quantum number.

**Hyperfine-coupling and g-factor from numerical electronic structure theory.** Spin-rotation constants and g-factors were computed from coupled-cluster response theory using London atomic orbitals and rotational London atomic orbitals<sup>60–63</sup>. As has been found before, the calculations are not very sensitive to the size of the basis set or core correlation<sup>60</sup>. At the minimum of the potential energy curve, computed values for  $g$  and  $c_{IJ}$  deviate by about 0.1% between CCSDT and CCSD(T), and still by less than 0.5% between CCSDT and CCSD, demonstrating well-converged results with respect to the cluster operator (see Extended Data Table 1). Results obtained with the  $3\zeta$  basis set cc-pVTZ differ substantially from those obtained with larger basis sets (13% for  $g$ ). The difference between the calculation with the largest and second-largest basis set (CCSD(T)/cc-pCV5Z and CCSD(T)/cc-pCVQZ) is 1.7% for  $g$  and 0.6% for  $c_{IJ}$ . In the literature, computed values based on a comparable level of theory usually deviate by less than 5% from experimental values, and often the deviation is less than 1% (refs 60, 64–66). On the basis of these results, we will use CCSD(T)/cc-pCV5Z to compute all properties and estimate the error on computed values of  $c_{IJ}$  and  $g$  to be  $\pm 5\%$ . The minimum of the potential energy curve at the CCSD(T)/cc-pCV5Z level of theory is  $r_0 = 1.896 \text{ \AA}$ , in agreement with ref. 25.

Vibrationally averaged values are obtained using the vibrational wavefunction and a polynomial interpolation of the property. Relativistic corrections to the spin-rotation constant from Thomas precession<sup>67</sup> were included, but are always small, of the order of 10 Hz. The results are presented in Extended Data Table 2. The vibrational corrections are smaller for the  $g$ -factor, because  $g(r)$  is approximately linear in the relevant range of  $r$ . Because the wavefunction of the vibrational ground state is, to a good approximation, as symmetric around the equilibrium distance  $r_0$  as is the harmonic approximation, the vibrational correction to any property that depends linearly on  $r$  nearly vanishes.

The behaviour of the spin-rotation constant and  $g$ -factor as a function of the bond distance is shown in Extended Data Figs 2 and 3.

**Magnetic sublevels of  $\text{CaH}^+$ .** The energies of the rotational levels of the molecule referenced to the electronic and vibrational ground state are approximately proportional to the eigenvalues of the square of the rotational angular momentum operator  $\hat{J}^2: \hbar R(J+1)$ . For a given rotational quantum number  $J$  and with a magnetic field  $\mathbf{B}$ , the energy of a state is further determined by the mutual (hyperfine) coupling between the orbital magnetic moment, produced by the charges rotating with the molecule, and the magnetic moment of the hydrogen nucleus (proportional to  $\hat{J} \cdot \hat{\mathbf{I}}$ ), as well as the coupling of the individual magnetic moments to the external magnetic field (proportional to  $\hat{J} \cdot \mathbf{B}$  and to  $\hat{\mathbf{I}} \cdot \mathbf{B}$ ), which split the levels by a few kilohertz. With the spin-rotation constant  $c_{IJ}$  and  $g$ -factor  $g$ , the structure of  $^{40}\text{CaH}^+$  magnetic sublevels in each  $J$  manifold can be calculated by diagonalizing the Hamiltonian:

$$\hat{H} = -g \frac{\mu_{\text{N}}}{\hbar} \hat{J} \cdot \mathbf{B} - g_{\text{I}} \frac{\mu_{\text{N}}}{\hbar} \hat{\mathbf{I}} \cdot \mathbf{B} - \frac{2\pi c_{IJ}}{\hbar} \hat{\mathbf{I}} \cdot \hat{J}$$

where  $g_{\text{I}}$  is the proton  $g$ -factor and  $\mu_{\text{N}}$  is the nuclear magneton. In our experiments, the external magnetic field defines the quantization axis,  $\mathbf{B} = B\mathbf{e}_{\tilde{z}}$ , where  $\mathbf{e}_{\tilde{z}}$  is a unit vector along the magnetic field direction (the  $\tilde{z}$  axis does not coincide with the  $z$  axis along which the ion crystal aligns; see Fig. 1) and  $B \approx 0.36 \text{ mT}$ . The molecule is neither in the Zeeman regime, in which the mutual coupling of the spins is stronger than their coupling to the external field, nor the Paschen–Back regime, in which the spins tend to align with the magnetic field. Defining the eigenvalues of  $\hat{J}_{\tilde{z}} + \hat{I}_{\tilde{z}}$  as  $\hbar m = \hbar(m_{\text{J}} + m_{\text{I}})$  and using the operator identity  $\hat{J}_{\tilde{x}}\hat{I}_{\tilde{x}} + \hat{J}_{\tilde{y}}\hat{I}_{\tilde{y}} = (\hat{J}_{\tilde{+}}\hat{I}_{\tilde{-}} + \hat{J}_{\tilde{-}}\hat{I}_{\tilde{+}})/2$ , where  $\hat{J}_{\tilde{\pm}}|J, m_{\text{J}}\rangle = \hbar\sqrt{(J \mp m_{\text{J}})(J \pm m_{\text{J}} + 1)}|J, m_{\text{J}} \pm 1\rangle$  act as ladder operators, provided that  $|m| \leq J$  (and likewise  $\hat{I}_{\tilde{\pm}}$ ), we can rewrite

$$\hat{H} = -\left(g\hat{J}_{\tilde{z}} + g_{\text{I}}\hat{I}_{\tilde{z}}\right) \frac{\mu_{\text{N}}}{\hbar} B - \frac{2\pi c_{IJ}}{\hbar} \left[\hat{J}_{\tilde{z}}\hat{I}_{\tilde{z}} + \frac{\hat{J}_{\tilde{+}}\hat{I}_{\tilde{-}} + \hat{J}_{\tilde{-}}\hat{I}_{\tilde{+}}}{2}\right]$$

This shows that, irrespective of the value of  $B$ ,  $m$  is a ‘good’ quantum number—that is, all terms in  $\hat{H}$  preserve  $m$ . For  $^{40}\text{CaH}^+$ , the nuclear spin of the proton is  $I = 1/2$  and the Hamiltonian is block-diagonal in the basis of product states  $|J, m_{\text{J}}\rangle|I, m_{\text{I}}\rangle$ . For the extreme cases  $m = \pm(J + 1/2)$ , the eigenstates of  $\hat{H}$  are  $|J, \pm(J + 1/2), \pm\rangle = |J, \pm J\rangle|1/2, \pm 1/2\rangle$ —fully aligned product states with energies  $E_{\pm(J+1/2), \pm} = \mp(g_{\text{I}} + g_{\text{J}}/2)\mu_{\text{N}}B \mp hc_{IJ}J/2$ . In all other cases, the blocks have dimensions  $2 \times 2$  of the form

$$\hat{H}_{J,m} = \begin{pmatrix} -\mu_{\text{N}}B\left[g\left(m - \frac{1}{2}\right) + \frac{g_{\text{I}}}{2}\right] - h\frac{c_{IJ}}{2}\left(m - \frac{1}{2}\right) & -h\frac{c_{IJ}}{2}\sqrt{\left(J + \frac{1}{2}\right)^2 - m^2} \\ -h\frac{c_{IJ}}{2}\sqrt{\left(J + \frac{1}{2}\right)^2 - m^2} & -\mu_{\text{N}}B\left[g\left(m + \frac{1}{2}\right) - \frac{g_{\text{I}}}{2}\right] + h\frac{c_{IJ}}{2}\left(m + \frac{1}{2}\right) \end{pmatrix}$$

When diagonalizing such a block in analogy to the solution of the Breit–Rabi equation, we get the eigenvectors

$$\begin{aligned} |J, m, +\rangle &= \sqrt{\frac{X-Y}{2X}} \left|J, m + \frac{1}{2}\right\rangle \left|\frac{1}{2}, -\frac{1}{2}\right\rangle + \sqrt{\frac{X+Y}{2X}} \left|J, m - \frac{1}{2}\right\rangle \left|\frac{1}{2}, \frac{1}{2}\right\rangle \\ |J, m, -\rangle &= -\sqrt{\frac{X+Y}{2X}} \left|J, m + \frac{1}{2}\right\rangle \left|\frac{1}{2}, -\frac{1}{2}\right\rangle + \sqrt{\frac{X-Y}{2X}} \left|J, m - \frac{1}{2}\right\rangle \left|\frac{1}{2}, \frac{1}{2}\right\rangle \end{aligned} \quad (3)$$

with

$$\begin{aligned} X &= \frac{1}{2} \sqrt{h^2 c_{IJ}^2 \left[ \left( J + \frac{1}{2} \right)^2 - m^2 \right] + [hc_{IJ}m - \mu_{\text{N}}B(g - g_{\text{I}})]^2} \\ Y &= -\mu_{\text{N}}B \left( \frac{g}{2} - \frac{g_{\text{I}}}{2} \right) - mh \frac{c_{IJ}}{2} \end{aligned}$$

The corresponding eigenvalues are

$$E_{m, \pm} = h \frac{c_{IJ}}{4} - \mu_{\text{N}}B g \quad m \mp X$$

The contribution from  $X$  can approximately cancel the other factors in  $E_{m, \pm}$ , leading to small and similar transition frequencies between states with different  $m$  in that manifold, whereas the  $m$ -dependent effects add up in  $E_{m, \pm}$  (shown for  $J = 1, 2$  in Fig. 2). We take advantage of small frequency differences in both manifolds to pump several substates simultaneously, while using the most distinguishable transitions  $|J, -J + 1/2, -\rangle \leftrightarrow |J, -J - 1/2, -\rangle$  for state determination and spectroscopy (see also Methods sections ‘Pumping of molecular states’). To simplify the expressions that contain the eigenstates in the main text, we use the abbreviation  $|\mathcal{J}\rangle$  as a shorthand for states with the set of quantum numbers  $|J, m, \xi\rangle$ , with  $\xi \in \{+, -\}$ .

**Stimulated Raman transitions.** Raman scattering on molecules usually involves a single light field at frequency  $\omega_1$  that is far off-resonant from all intermediate excited states  $|f\rangle$ . The second, Stokes or anti-Stokes photon at  $\omega_2$  is then spontaneously emitted by the molecule, as shown in Extended Data Fig. 4a. In our experiments, we excite transitions from  $|a\rangle$  to  $|b\rangle$  in such a way that the second photon at  $\omega_2$  is stimulated by a second driving field at that frequency, as shown schematically in Extended Data Fig. 4b. The second field greatly enhances the Raman scattering rate and leads to coherent transitions between  $|a\rangle$  and  $|b\rangle$ . The two driving light fields are characterized by frequency  $\omega_n$  ( $n = \{1, 2\}$ ), field amplitude  $|E_n|$  and polarization  $\hat{\mathbf{q}}^{(n)} = q_{-1}^{(n)}\sigma^- + q_0^{(n)}\pi + q_1^{(n)}\sigma^+$ , with  $|\hat{\mathbf{q}}^{(n)}|^2 = 1$ , where  $\pi$  is oriented along the quantizing magnetic field and  $\sigma^+$  ( $\sigma^-$ ) is the circular polarization rotating clockwise (anticlockwise) around that direction when viewed along the wavevector. The fields are far off-resonant from the smallest frequency difference between states of the molecule with the electrons in the ground state and those with electrons in excited states.

Although each light field is very far-detuned from resonance, we assume that the frequency difference  $\Delta\omega = (\omega_2 - \omega_1)$  is close to the frequency difference  $\omega_0 = (E_b - E_a)/\hbar$  of the initial molecular state  $|a\rangle$  and a final state  $|b\rangle$ . The Raman–Rabi frequency  $\Omega_{ab}$  for a stimulated Raman transition can then be approximated in perturbation theory as

$$\Omega_{ab} = \frac{1}{4\hbar^2} \sum_f \frac{\langle b | \mathbf{e} \cdot \mathbf{E}_2 | f \rangle \langle f | \mathbf{e} \cdot \mathbf{E}_1 | a \rangle}{\omega_{af} - \omega_1} + \frac{\langle b | \mathbf{e} \cdot \mathbf{E}_1 | f \rangle \langle f | \mathbf{e} \cdot \mathbf{E}_2 | a \rangle}{\omega_{af} + \omega_2} \quad (4)$$

where  $e$  is the charge of the electron,  $\mathbf{r}$  its position (we have neglected the sum over indistinguishable electrons for simplicity) and  $\omega_{af} = (E_f - E_a)/\hbar$  is the frequency difference between the initial state  $|a\rangle$  and an intermediate state  $|f\rangle$ . The term in the sum with denominator  $\omega_{af} - \omega_1$  is due to terms rotating at the difference frequency between the first light field and the energy difference of initial and intermediate states. In most textbook discussions, the difference is assumed to be much smaller than the sum  $\omega_{af} + \omega_2$  that appears in the denominator of the other term. In these cases, terms in the perturbation expansion co-rotating at this sum are neglected with respect to the counter-rotating terms at the difference frequency, in what is called the rotating-wave approximation. However, in our experiments, the light fields are detuned so far that the ratio of difference to sum is approximately 1:2.3 for laser light near 1,051 nm, if we estimate the energy difference of the ground and first excited electronic levels according to ref. 25. Therefore, we cannot necessarily neglect the co-rotating terms. The difference in the processes is illustrated in Extended Data Fig. 4c: for the counter-rotating terms (red arrows), the photon at frequency  $\omega_1$  is absorbed to set up a coherence in the molecule that rotates at  $\omega_{af} - \omega_1$ , and then a photon at  $\omega_2$  is stimulated; in the co-rotating term (blue arrows), the photon at  $\omega_2$  is stimulated first, setting up a coherence at the larger detuning  $\omega_{af} + \omega_2$ , after which the photon at  $\omega_1$  is absorbed, leading to the same resonance condition and selection rules as in the counter-rotating term.

In our experiments, initial and final states are in the electronic ground state ( $|1^1\Sigma\rangle$  in the notation of ref. 25), vibrational ground state ( $v=0$ ), and a particular manifold of the rotation characterized by quantum number  $J$ . To determine the Raman Rabi rate, we need to evaluate dipole matrix elements of the form

$$\langle f|e\mathbf{r}\cdot\mathbf{E}|s\rangle = e|\mathbf{E}| \langle \Psi_{f,v}|r|1^1\Sigma, v=0\rangle \langle \Phi_f(\theta, \phi)|\hat{\mathbf{r}}\cdot\hat{\mathbf{q}}|\Phi_s(\theta, \phi)\rangle$$

where  $s \in \{a, b\}$ ,  $r = |\mathbf{r}|$  and  $\hat{\mathbf{r}} = \mathbf{r}/r$ . On the right-hand side we have factored the molecular wavefunctions into two parts. The radial part of the electronic wavefunction of the excited state  $\Psi_{f,v}$  depends only on the internuclear distance  $h$  and the vibrational quantum number  $v$ . The angular part of the wavefunction  $\Phi_s(\theta, \phi)$  depends only on the two angle coordinates,  $\theta$  and  $\phi$ . Such a separation of variables can be justified, for example, within the Born–Oppenheimer approximation. Here, we consider only the lowest excited electronic state  $|2^1\Sigma\rangle$  and neglect the differences in  $\omega_{af}$  due to the rotational and vibrational states,  $\omega_{af} \approx (E_{2^1\Sigma} - E_{1^1\Sigma})/\hbar \equiv \bar{\omega}$ . Under these assumptions we can rewrite equation (4) as

$$\begin{aligned} \Omega_{ab} &= \mathcal{E}(S_- + S_+) \\ \mathcal{E} &= \frac{e^2|\mathbf{E}_1||\mathbf{E}_2|}{4\hbar^2(\bar{\omega} - \omega_1)} \sum_{v'} |\langle \Psi_{2^1\Sigma, v'}|r|\Psi_{1^1\Sigma, 0}\rangle|^2 \\ S_- &= \sum_f \langle \Phi_b|\hat{\mathbf{r}}\cdot\hat{\mathbf{q}}^{(2)}|\Phi_f\rangle \langle \Phi_f|\hat{\mathbf{r}}\cdot\hat{\mathbf{q}}^{(1)}|\Phi_a\rangle \\ S_+ &= \frac{\bar{\omega} - \omega_1}{\bar{\omega} + \omega_1} \sum_f \langle \Phi_b|\hat{\mathbf{r}}\cdot\hat{\mathbf{q}}^{(1)}|\Phi_f\rangle \langle \Phi_f|\hat{\mathbf{r}}\cdot\hat{\mathbf{q}}^{(2)}|\Phi_a\rangle \end{aligned} \quad (5)$$

where we have also neglected the small frequency differences between the driving fields ( $\omega_1 \approx \omega_2$ ) in the denominators. Under these approximations,  $\mathcal{E}$  is a prefactor that is the same for all transitions considered and is approximately proportional to the sum over the squares of all Franck–Condon factors of vibrational states bound in the well of the first excited electronic state.

The position operator  $\mathbf{r}$  couples eigenstates of the rotational angular momentum  $|J, m_J\rangle$  and has no effect on the eigenstates of the proton nuclear spin  $|I, m_I\rangle$ . Therefore, it is convenient to use the product basis  $|J, m_J\rangle|I, m_I\rangle$  with the nuclear spin  $I$  fixed. In  $^{40}\text{CaH}^+$ , the nuclear spin  $I = 1/2$  is that of the proton. The sum over the intermediate states  $\Phi_f$  in  $S_-$  is

$$S_- = \sum_{J, m_J, m_I} \langle \Phi_b|\hat{\mathbf{r}}\cdot\hat{\mathbf{q}}^{(2)}|J, m_J\rangle|I, m_I\rangle \langle J, m_J|I, m_I\rangle \langle I, m_I|\hat{\mathbf{r}}\cdot\hat{\mathbf{q}}^{(1)}|\Phi_a\rangle \quad (6)$$

The sum of angular momenta in the  $z$  direction,  $m_s = m_J + m_I$  remains a good quantum number for all values of the magnetic field  $\mathbf{B} = B\hat{\mathbf{e}}_z$ . This implies that we can write the eigenstates as

$$|\Phi_s\rangle = \sum_{m_I} c_{m_I}^{(s)} |J, m_s - m_I, 1/2, m_I\rangle \quad (7)$$

where  $s \in \{a, b\}$  and  $c_{m_I}^{(s)}$  are the coefficients of the eigenstates derived in equation (3). Substituting equation (7) into equation (6) yields

$$S_- = \sum_{J, m_J, m_I} c_{m_I}^{(b)} c_{m_I}^{(a)} \langle J_b, m_b - m_I|\hat{\mathbf{r}}\cdot\hat{\mathbf{q}}^{(2)}|J, m_J\rangle \langle J, m_J|I, m_I\rangle \langle I, m_I|\hat{\mathbf{r}}\cdot\hat{\mathbf{q}}^{(1)}|J_a, m_a - m_I\rangle$$

We can express  $\hat{\mathbf{r}}$  as a vector in the spherical basis to write out the scalar product and use the Wigner–Eckart theorem to determine the matrix element for photon absorption from a field with polarization  $\hat{\mathbf{q}}$ :

$$\langle J, m|\hat{\mathbf{r}}\cdot\hat{\mathbf{q}}|J', m'\rangle = \sqrt{\max(J, J')} (J - J') \sum_{k=-1}^1 \hat{q}_k (-1)^{k+J-m} \begin{pmatrix} J & 1 & J' \\ -m & k & m' \end{pmatrix} \quad (8)$$

where the  $2 \times 3$  array is a Wigner  $3J$  symbol. The right-hand side implies the usual dipole selection rules, which reduce the number of excited states that need to be considered in the Raman–Rabi frequency as well as the final states that can have a non-zero coupling to  $|\Phi_a\rangle$ . In particular,  $\Delta J = J_b - J_a = 0, \pm 2$  and  $\Delta m = m_b - m_a = 0, \pm 1, \pm 2$ . Restricting the sums with the selection rules and setting  $m_a = m_a - m_I$ , we get

$$\begin{aligned} S_- &= \sum_{m_I=-1/2}^{1/2} \sum_{k_1, k_2=-1}^1 c_{m_I}^{(b)} c_{m_I}^{(a)} \left[ \langle J_a - 1, m_{J_a} + k_1|\hat{\mathbf{r}}_{k_1} q_{k_2}^{(2)}|J_b, m_{J_a} + k_1 - k_2\rangle \right. \\ &\quad \langle J_a - 1, m_{J_a} + k_1|\hat{\mathbf{r}}_{k_1} q_{k_1}^{(1)}|J_a, m_{J_a}\rangle + \\ &\quad \langle J_a + 1, m_{J_a} + k_1|\hat{\mathbf{r}}_{k_2} q_{k_2}^{(2)}|J_b, m_{J_a} + k_1 - k_2\rangle \times \\ &\quad \left. \langle J_a + 1, m_{J_a} + k_1|\hat{\mathbf{r}}_{k_1} q_{k_1}^{(1)}|J_a, m_{J_a}\rangle \right] \end{aligned} \quad (9)$$

with the matrix elements all written in the form in which the photon is absorbed, to be compatible with equation (8). The expressions for  $S_+$  are calculated in the same way, but the available intermediate states change because the photon from field  $\mathbf{E}_2$  and its angular momentum is absorbed first in those terms.

AC Stark shifts arise as a result of Raman transitions with  $|a\rangle = |b\rangle$ , and amount to an energy shift of state  $|a\rangle$  by  $\Delta E_{AC} = \hbar\Omega_{aa}$ . If the two driving fields have different frequencies and/or polarizations, then both photons contributing to a Raman transition need to come from the same field to conserve energy and angular momentum. For two fields with polarizations  $\hat{\mathbf{q}}^{(1)}$  and  $\hat{\mathbf{q}}^{(2)}$ , and setting  $J_a = J$ ,  $m_a = m$  and  $c_{m_I}^{(a)} = c_{m_I}$ , we can simplify equation (5) to

$$\begin{aligned} \Delta E_{AC} &= (\mathcal{E}_1 + \mathcal{E}_2) S_- \frac{2\bar{\omega}}{\bar{\omega} - \omega_1} \\ &= \frac{2\bar{\omega}}{\bar{\omega} - \omega_1} \sum_{n=1}^2 \mathcal{E}_n \\ &\quad \sum_{m_I=-1/2}^{1/2} |c_{m_I}|^2 \left[ \frac{(m + m_I)^2 (3|q_0^{(n)}|^2 - 1)}{3 - 4J(J+1)} + \frac{1 - J(J+1)(|q_0^{(n)}|^2 + 1)}{3 - 4J(J+1)} \right] \end{aligned}$$

The AC Stark shift can be made state-independent in several ways; for example, choosing  $|q_0^{(n)}|^2 = 1/3$  yields

$$\Delta E_{AC} = (\mathcal{E}_1 + \mathcal{E}_2) \frac{2\bar{\omega}}{3(\bar{\omega} - \omega_1)}$$

In our experiments, we chose the polarizations of one field, described by  $\mathcal{E}_1$ , to be linear ( $|q_0^{(1)}|^2 = 1$ ), and those of the other field to be circular ( $|q_0^{(2)}|^2 = 0$ ), with twice the intensity of the linearly polarized field ( $\mathcal{E}_2 = 2\mathcal{E}_1$ ). In this case, the AC Stark shift is also state independent:

$$\Delta E_{AC} = \mathcal{E}_1 \frac{2\bar{\omega}}{(\bar{\omega} - \omega_1)}$$

In both cases, the AC Stark shifts produce a global shift of all energy levels under the assumption of large laser detuning. The global shift will not affect the eigenstates of the Hamiltonian; therefore, the eigenstates are not changed when the light fields are turned on and off, and the observed transition frequencies, which are proportional to energy differences, are not altered by the AC Stark shifts. The validity of this approximation can be estimated by looking at the relative difference between energy denominators in equation (4). The contributing intermediate states are  $J+1$  and  $J-1$ ; therefore, the energy differs by  $\Delta E = \hbar R(2+4J) \leq 26\hbar R$  for  $J \leq 6$ , yielding  $\Delta E \approx h \times 3.74$  THz for  $J=6$ . The laser detuning from the energy difference between the ground state and the vibrational ground state in the first excited electronic state is roughly  $h \times 430.8$  THz (ref. 25). Therefore, all energy denominators deviate by less than 1%.

In the experiment, the intensities of the  $\sigma$  and  $\pi$  beams are calibrated with the AC Stark shifts on the  $|S, m_F = -1/2\rangle \leftrightarrow |D, m_F = -5/2\rangle$  transition. During the calibration, the ion order is switched such that the  $^{40}\text{Ca}^+$  ion is where the  $^{40}\text{CaH}^+$  would be in the spectroscopy experiments. The power in both beams is actively controlled to yield stable Stark shifts during experiments. AC Stark shifts of 200 kHz and 130 kHz for the  $\sigma^-$ - and  $\pi$ -polarized beams are used in the sideband pulses. We experimentally find minimal shifts in the transition frequencies inferred from sideband and carrier measurements at the ratio of 2:1.3 for the Stark shifts on  $^{40}\text{Ca}^+$ .

**Trap parameters.** The ions are trapped in a linear Paul trap consisting of two wafers with segmented DC electrodes; details of the trap construction are available in ref. 68. The secular frequencies for single  $^{40}\text{Ca}^+$  ions are  $\{\nu_x, \nu_y, \nu_z\} = \{4.567, 7.546, 3.000\}$  MHz. In the experiment, the order of the two-ion crystal is monitored and maintained to be the same throughout to improve the consistency of laser-beam illumination and micro-motion compensation during the experiments. **Sympathetic ground-state cooling.** Ground-state cooling before the spectroscopy experiments is achieved by an initial stage of Doppler cooling with the 397-nm  $\pi$  beam (blue arrow perpendicular to the magnetic field in Fig. 1), followed by electromagnetically induced transparency cooling with the 397-nm  $\pi$  and  $\sigma$  beams (blue arrow parallel with the magnetic field)<sup>69</sup>. Finally, we perform resolved sideband cooling of the in-phase and out-of-phase modes in the  $z$  direction and the lower-frequency (about 3.4 MHz) out-of-phase rocking mode in the  $x$  direction with the 729-nm beam (red arrow perpendicular to the  $\mathbf{B}$  field). We use the  $z$  out-of-phase mode with low ( $< 1$  quanta per 100 ms) heating rate for quantum-logic readout with low false-positive error rates. The  $x$  rocking mode is cooled to the ground state to avoid adverse effects from the parametric coupling between that mode and the readout mode<sup>70</sup>. The  $D_{5/2}$  and  $D_{3/2}$  states are repumped by the 854-nm and 866-nm beams (pink arrows perpendicular to the  $\mathbf{B}$  field in Fig. 1).

**Pumping of molecular states.** The room-temperature environment in our experiment equilibrates the  $^{40}\text{CaH}^+$  population with the background blackbody radiation such that it is in the electronic and vibrational ground state with very high probability (>99%). The populations in the rotational levels are thermally distributed. For  $^{40}\text{CaH}^+$  in  $B \approx 0.36$  mT, the frequencies of most  $|J, m, \xi\rangle \rightarrow |J, m-1, \xi\rangle$  transitions, with  $\xi \in \{+, -\}$ , fall into narrow regions around  $-2$  kHz and  $-6$  kHz, respectively. Pumping of the molecular population can be achieved by driving the out-of-phase blue sideband of those transitions, followed by out-of-phase mode sideband cooling pulses on  $^{40}\text{Ca}^+$  (ref. 6). The population is pumped towards the  $-(J \pm 1/2)$  ends by ensuring that the frequency of the 1,051-nm  $\sigma^-$  beam is higher than that of the  $\pi$  beam by the out-of-phase mode frequency,  $\nu_1 \approx 5.164$  MHz, plus the frequency of the transition with  $\Delta m = -1$  to be driven. Pumping of the spectroscopically resolved transitions  $|J, -J+1/2, +\rangle \leftrightarrow |J, -J+3/2, -\rangle$  and  $|J, -J-1/2, -\rangle \leftrightarrow |J, -J+1/2, -\rangle$  is interspersed to accumulate all of the molecular population in the states  $|J, -J+1/2, -\rangle$  (see Fig. 2 for  $J \in \{1, 2\}$ ).

The pumping pulses from the 1,051-nm beams do not change the rotation quantum number  $J$ , and thus maintain the equilibrium population in each  $J$  manifold dictated by the background blackbody radiation.

**Projective purification of imperfect  $\text{Ca}^+$  state preparation.** To achieve a low false-positive error rate in the experiment, imperfect  $^{40}\text{Ca}^+$  state preparation and ground-state cooling are purified by exploiting the high detection fidelity in  $^{40}\text{Ca}^+$  state determination. With fluorescence count rates of more than  $2 \times 10^5$  and less than  $4 \times 10^3$  counts per second when the  $^{40}\text{Ca}^+$  is in the  $|S\rangle$  and  $|D\rangle$  states, respectively, the detection fidelity can be  $>0.9999$  (ref. 27). The target state,  $|D\rangle|0\rangle$ , is prepared via two purification stages. First, after ground-state cooling, a carrier  $\pi$  pulse converts  $|S\rangle$  to  $|D\rangle$ . If the  $^{40}\text{Ca}^+$  is found to be bright in the subsequent detection pulse, then the state preparation starts over. Otherwise, the second purification stage follows, wherein a blue-sideband  $\pi$  pulse converts  $|D\rangle|1\rangle$  to  $|S\rangle|0\rangle$ , but leaves  $|D\rangle|0\rangle$  unaffected. The subsequent detection pulse would signal most of the population not in  $|0\rangle$  with a bright outcome, and state preparation would start again from the beginning. The two dark outcomes from the first two purification stages leave the population mostly in  $|D\rangle|0\rangle$ , and the ions are ready for a spectroscopy experiment. The spectroscopy pulse on the molecule deposits a quantum of motion in the out-of-phase mode if successful, or leaves that mode in the ground state otherwise. The spectroscopy pulse on the molecule is followed by a blue-sideband  $\pi$  pulse on the atomic ion, transforming  $|D\rangle|1\rangle$  to  $|S\rangle|0\rangle$ . A bright outcome in the final detection pulse signals the creation of a phonon in the out-of-phase mode as a result of the spectroscopy pulse. A flow chart for the sequence is shown in Extended Data Fig. 5. Using the purifying preparation sequence, false-positive errors can be reduced to about 0.5% for spectroscopy experiments shorter than 1.5 ms. A similar sequence is also implemented when the  $|D\rangle|1\rangle$  state is prepared before the spectroscopy pulse. Heating increases the false-positive error rates with increasing duration of the spectroscopy experiments.

**Experimental sequences for repetitive projective state preparation, Rabi spectroscopy, and Ramsey fringes.** Coherent spectra, Rabi flopping and Ramsey fringes were obtained by repeating experimental sequences consisting of projective state preparation, molecular spectroscopy pulses and state detection. The experiment control system attempts to keep track of the current state of the molecule. In the preparation stage, pumping is applied periodically if the rotational state of the molecule is unknown. Between pumping, projective state preparation for various  $J$  manifold is attempted by applying Raman sideband  $\pi$  pulses to drive the  $|\mathcal{T}_J\rangle|0\rangle \leftrightarrow |J, -J-1/2, -\rangle|1\rangle$  transition and detecting the results. A positive event prompts subsequent projective state preparation attempts for the same  $J$ . We require at least two consecutive positive events signalling the transitions  $|\mathcal{T}_J\rangle|0\rangle \leftrightarrow |J, -J-1/2, -\rangle|1\rangle$  before the experiment control signals the successful preparation of the molecule in  $|J, -J-1/2, -\rangle$ . The repetitive projection filters the false-positive events and thus achieves higher fidelity in projective state preparation. If four consecutive negative events are registered, then the experiment control determines that the molecule is not in the corresponding manifold and switches to attempt state preparation on a target transition with different  $J$ . After the projective state preparation is heralded, the state of the  $^{40}\text{Ca}^+$  ion and the motional mode are prepared in  $|D\rangle|0\rangle$ . For the coherent spectra and Rabi flopping, we apply the carrier pulse with variable  $\Delta\nu$  and pulse duration, respectively, to drive the  $|J, -J-1/2, -\rangle \leftrightarrow |\mathcal{T}_J\rangle$  transition. For the Ramsey fringes, two carrier  $\pi/2$  pulses on the transition are applied, separated by a delay of duration  $T$ , with variable relative phase between the two pulses. We then detect whether the molecule has made the transition to  $|\mathcal{T}_J\rangle = |J, -J+1/2, -\rangle$ . A sideband  $\pi$  pulse on the molecular  $|\mathcal{T}_J\rangle|0\rangle \leftrightarrow |J, -J-1/2, -\rangle|1\rangle$  transition and then a sideband pulse that drives the  $|D\rangle|1\rangle \rightarrow |S\rangle|0\rangle$  transition in  $^{40}\text{Ca}^+$  are applied. The state detection ends with a fluorescence detection, with the outcome  $|S\rangle$  signalling a positive molecular transition event. We measure the transition probabilities by repeating the sequence.

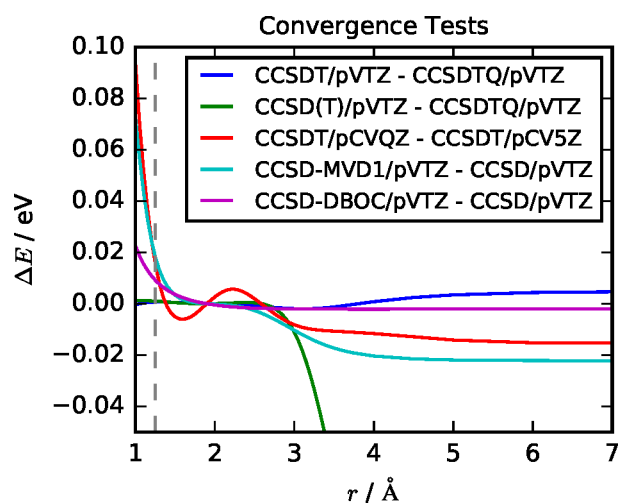
**Comparison of calculated and experimental molecular transition parameters.** We presented spectroscopy experiments on the motional sidebands of the  $|\mathcal{T}_J\rangle \leftrightarrow |J, -J-1/2, -\rangle$  transitions (Fig. 3), as well as carrier transitions (Fig. 4). Determination of energy differences based on the carrier transitions should reduce systematic uncertainties as compared with sideband transitions for two reasons: (i) drifts of the secular frequency over time do not contribute to the uncertainties in the measured resonance frequencies; and (ii) for a given Rabi rate, the light intensity on a carrier transition can be reduced by a factor of  $\eta$  (the Lamb–Dicke parameter) compared with a sideband transition. This greatly reduces the differential AC Stark shift induced by the probe laser beams. Extended Data Table 3 lists the experimental carrier transition frequencies for the rotational manifolds  $J=1, 2, \dots, 6$  at 1/8 of the light intensity used for the sideband transitions shown in Fig. 3, as well as the predictions from our theoretical model. Experimental errors are purely statistical and theoretical uncertainties are based on the assumption that uncertainties in the parameters  $c_J$  and  $g$  add like random and independent variables. Although the close agreement between experimental frequencies and calculated frequencies supports our identification of the transitions, we are unable to perform a quantitative comparison. Such a comparison would require careful characterization of systematic uncertainties in the experiment and of correlations between the theoretical uncertainties.

We also compared the experimentally determined Rabi rates from the Rabi flopping curves in Fig. 4 with theory. For the probed transitions in the  $J=1$  and  $J=2$  manifolds, we find Rabi rates of  $\Omega_{J=1} = 2\pi \times 2.078(14)$  kHz and  $\Omega_{J=2} = 2\pi \times 1.804(12)$  kHz, respectively (uncertainties are statistical). The ratio of the two is 1.152(11), in reasonable agreement with the value of 1.132 predicted by equations (5) and (9).

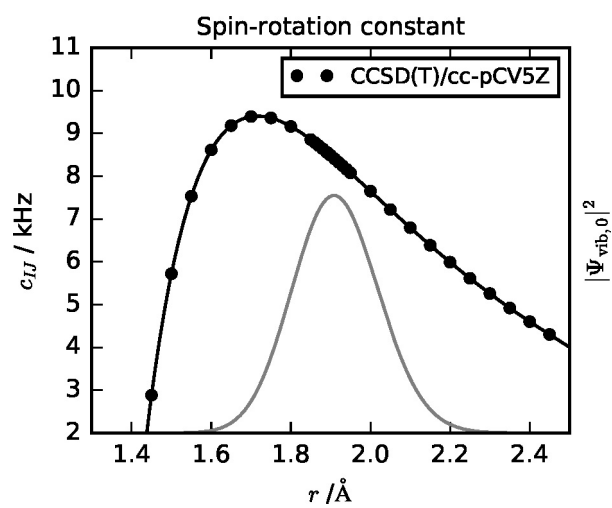
**Data availability.** Data are available from the corresponding author on request.

- Cornell, E. A. & Wieman, C. E. Nobel Lecture: Bose–Einstein condensation in a dilute gas, the first 70 years and some recent experiments. *Rev. Mod. Phys.* **74**, 875–893 (2002).
- Ketterle, W. Nobel Lecture: When atoms behave as waves: Bose–Einstein condensation and the atom laser. *Rev. Mod. Phys.* **74**, 1131–1151 (2002).
- DeMarco, B. & Jin, D. S. Onset of Fermi degeneracy in a trapped atomic gas. *Science* **285**, 1703–1706 (1999).
- O'Hara, K. M. *et al.* Ultrastable  $\text{CO}_2$  laser trapping of lithium fermions. *Phys. Rev. Lett.* **82**, 4204–4207 (1999).
- DeMille, D. Diatomic molecules, a window onto fundamental physics. *Phys. Today* **68**, 34–40 (2015).
- Koelmeij, J. C. J., Roth, B., Wicht, A., Ernsting, I. & Schiller, S. Vibrational spectroscopy of  $\text{HD}^+$  with 2-ppb accuracy. *Phys. Rev. Lett.* **98**, 173002 (2007).
- Flambaum, V. & Kozlov, M. Enhanced sensitivity to the time variation of the fine-structure constant and  $m_p/m_e$  in diatomic molecules. *Phys. Rev. Lett.* **99**, 150801 (2007).
- Pupillo, G., Micheli, A., Büchler, H.-P. & Zoller, P. in *Cold Molecules: Theory, Experiment, Applications* (eds Krems, R. *et al.*) Ch. 12 (CRC Press, 2009).
- DeMille, D. Quantum computation with trapped polar molecules. *Phys. Rev. Lett.* **88**, 067901 (2002).
- Will, S. A., Park, J. W., Yan, Z. Z., Loh, H. & Zwerlein, M. Coherent microwave control of ultracold  $\text{Na}^{23}\text{K}^{40}$  molecules. *Phys. Rev. Lett.* **116**, 225306 (2016).
- Hudson, E. R. Method for producing ultracold molecular ions. *Phys. Rev. A* **79**, 032716 (2009).
- Lazarou, C., Keller, M. & Garraway, B. M. Molecular heat pump for rotational states. *Phys. Rev. A* **81**, 013418 (2010).
- Mur-Petit, J. *et al.* Temperature-independent quantum logic for molecular spectroscopy. *Phys. Rev. A* **85**, 022308 (2012).
- Shi, M., Herskind, P. F., Drewsen, M. & Chuang, I. L. Microwave quantum logic spectroscopy and control of molecular ions. *New J. Phys.* **15**, 113019 (2013).
- Rugango, R. *et al.* Sympathetic cooling of molecular ion motion to the ground state. *New J. Phys.* **17**, 035009 (2015).
- Ubachs, W., Koelmeij, J. C. J., Eikema, K. S. E. & Salumbides, E. J. Physics beyond the standard model from hydrogen spectroscopy. *J. Mol. Spectrosc.* **320**, 1–12 (2016).
- Schiller, S., Bakalov, D. & Korobov, V. I. Simplest molecules as candidates for precise optical clocks. *Phys. Rev. Lett.* **113**, 023004 (2014).
- Karr, J.-Ph.  $\text{H}_2^+$  and  $\text{HD}^+$ : candidates for a molecular clock. *J. Mol. Spectrosc.* **300**, 37–43 (2014).
- Blythe, P., Roth, B., Fröhlich, U., Wenz, H. & Schiller, S. Production of ultracold trapped molecular hydrogen ions. *Phys. Rev. Lett.* **95**, 183002 (2005).
- Kajita, M., Gopakumar, G., Abe, M. & Hada, M. Characterizing variation in the proton-to-electron mass ratio via precise measurements of molecular vibrational transition frequencies. *J. Mol. Spectrosc.* **300**, 99–107 (2014).
- Bely, K. *et al.* Rotational spectrum of the molecular ion  $\text{NH}^+$  as a probe for  $\alpha$  and  $m_e/m_p$  variation. *Phys. Rev. A* **83**, 062514 (2011).
- Kajita, M., Gopakumar, G., Abe, M., Hada, M. & Keller, M. Test of  $m_e/m_p$  changes using vibrational transitions in  $\text{N}_2^+$ . *Phys. Rev. A* **89**, 032509 (2014).

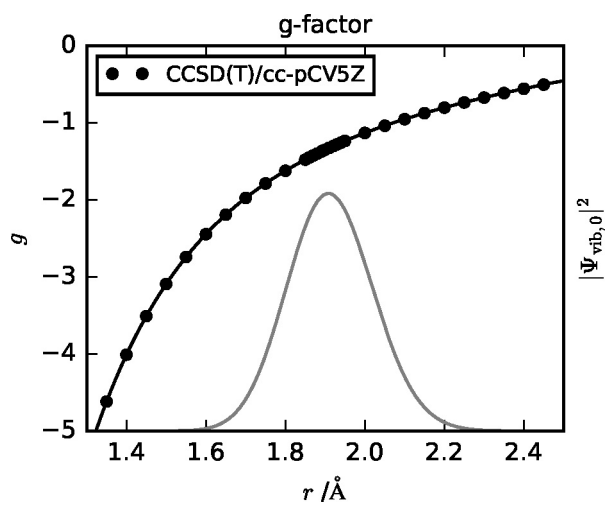
52. Hanneke, D., Carollo, R. A. & Lane, D. A. High sensitivity to variation in the proton-toelectron mass ratio in  $O_2^+$ . *Phys. Rev. A* **94**, 050101 (2016).
53. Pašteka, L. F., Borschevsky, A., Flambaum, V. V. & Schwerdtfeger, P. Search for the variation of fundamental constants: strong enhancements in  $X^{2II}$  cations of dihalogens and hydrogen halides. *Phys. Rev. A* **92**, 012103 (2015).
54. Stanton, J. F. *et al.* *CFOUR, coupled-cluster techniques for computational chemistry* <http://www.cfour.de> (2017).
55. Kállay, M. *et al.* *MRCC* <http://www.mrcc.hu> (2017).
56. Rolik, Z., Szegedy, L., Ladjánszki, I., Ladóczki, B. & Kállay, M. An efficient linear-scaling CCSD(T) method based on local natural orbitals. *J. Chem. Phys.* **139**, 094105 (2013).
57. Pople, J. A., Head-Gordon, M. & Raghavachari, K. Quadratic configuration interaction: a general technique for determining electron correlation energies. *J. Chem. Phys.* **87**, 5968–5975 (1987).
58. Dunning, T. H. Gaussian basis sets for use in correlated molecular calculations. I. The atoms boron through neon and hydrogen. *J. Chem. Phys.* **90**, 1007–1023 (1989).
59. Koput, J. & Peterson, A. A. Ab initio potential energy surface and vibrational-rotational energy levels of  $X^{2\Sigma^+}$  CaOH. *J. Phys. Chem. A* **106**, 9595–9599 (2002).
60. Gauss, J., Ruud, K. & Kállay, M. Gauge-origin independent calculation of magnetizabilities and rotational  $g$  tensors at the coupled-cluster level. *J. Chem. Phys.* **127**, 074101 (2007).
61. Gauss, J., Ruud, K. & Helgaker, T. Perturbation-dependent atomic orbitals for the calculation of spin-rotation constants and rotational  $g$  tensors. *J. Chem. Phys.* **105**, 2804–2812 (1996).
62. Puzzarini, C., Stanton, J. F. & Gauss, J. Quantum-chemical calculation of spectroscopic parameters for rotational spectroscopy. *Int. Rev. Phys. Chem.* **29**, 273–367 (2010).
63. Helgaker, T. *et al.* Recent advances in wave function-based methods of molecular-property calculations. *Chem. Rev.* **112**, 543–631 (2012).
64. Gauss, J. & Sundholm, D. Coupled-cluster calculations of spin-rotation constants. *Mol. Phys.* **91**, 449–458 (1997).
65. Jaszuński, M. *et al.* Spin-rotation and NMR shielding constants in HCl. *J. Chem. Phys.* **139**, 234302 (2013).
66. Amano, T. The Zeeman effect and hyperfine interactions in  $J = 1-0$  transitions of  $CH^+$  and its isotopologues. *J. Chem. Phys.* **133**, 244305 (2010).
67. Sundholm, D., Gauss, J. & Schäfer, A. Rovibrationally averaged nuclear magnetic shielding tensors calculated at the coupled-cluster level. *J. Chem. Phys.* **105**, 11051–11059 (1996).
68. Leibfried, D. *et al.* Creation of a six-atom Schrödinger cat state. *Nature* **438**, 639–642 (2005).
69. Morigi, G., Eschner, J. & Keitel, C. H. Ground state laser cooling using electromagnetically induced transparency. *Phys. Rev. Lett.* **85**, 4458–4461 (2000).
70. Roos, C. F. *et al.* Nonlinear coupling of continuous variables at the single quantum level. *Phys. Rev. A* **77**, 040302(R) (2008).



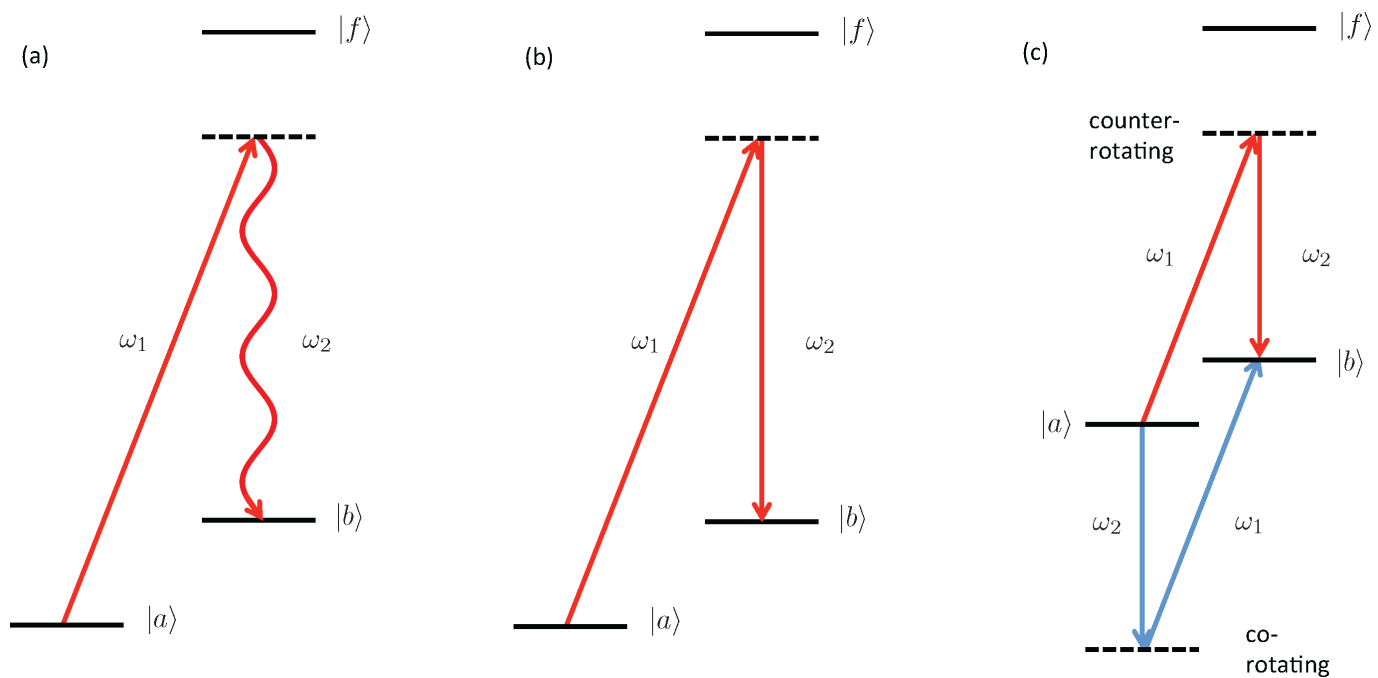
**Extended Data Figure 1 | Difference in energies  $\Delta E$  obtained with different methods.** All curves have been shifted to be zero at  $r = 1.896 \text{ \AA}$ . The grey dashed line is drawn at  $1.25 \text{ \AA}$ —the lower limit of a substantial probability density at a high vibrational quantum number ( $v = 10$ ). Basis sets are correlation-consistent basis sets (the 'cc' has been omitted for clarity). For  $r > 3.0 \text{ \AA}$ , which is outside of the range that is relevant for the electronic and vibrational ground state, CCSD(T) starts to deviate substantially from CCSDT, and deviations lie outside of the energy scale. MVD1, mass-velocity and one-electron Darwin correction; DBOC, diagonal Born-Oppenheimer correction.



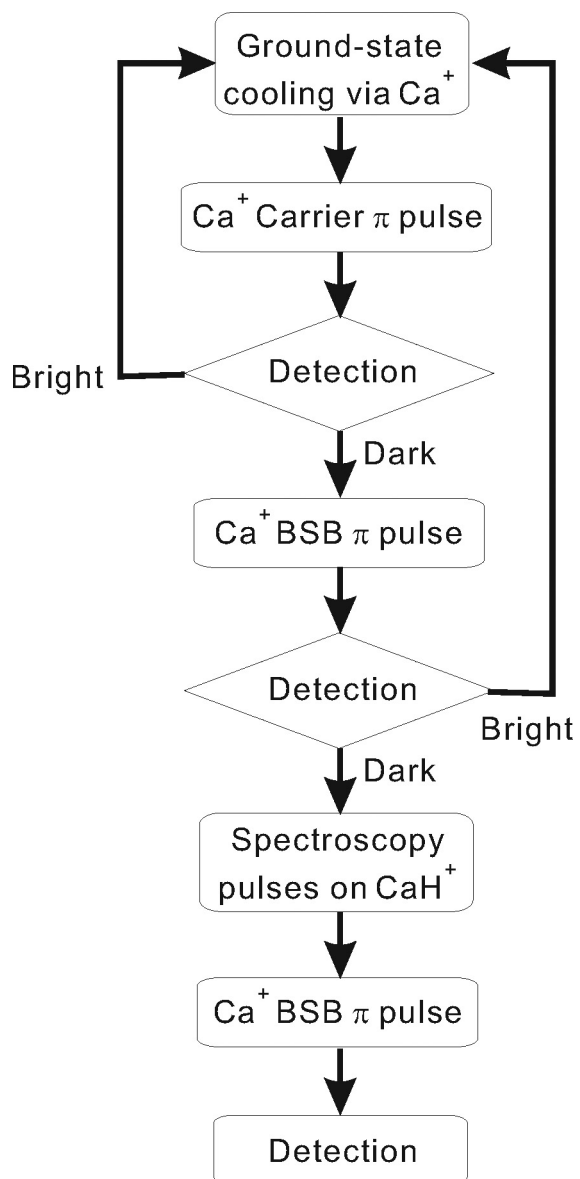
Extended Data Figure 2 | Spin-rotation factor  $c_{IJ}$ , fitted with an eighth-order polynomial. The squared vibrational wavefunction  $|\Psi_{vib,0}|^2$  is shown in grey for  $J=0$ .



**Extended Data Figure 3** | g-factor  $g$  fitted with an eighth-order polynomial. The squared vibrational wavefunction  $|\Psi_{\text{vib},0}|^2$  is shown in grey for  $J=0$ .



**Extended Data Figure 4 | Raman transitions.** **a**, Single-field Raman transition; a photon at frequency  $\omega_2$  is spontaneously emitted. **b**, Stimulated Raman transition, driven by two fields; a photon at  $\omega_2$  is stimulated by the second driving field. **c**, Order of absorption and emission, and detuning of the coherence in the counter-rotating (red) and co-rotating (blue) cases.



Extended Data Figure 5 | Flow chart of the purification stages.

**Extended Data Table 1 | Numerical values of the spin-rotation constant  $c_{IJ}$  and g-factor  $g$  at  $r_0 = 1.896 \text{ \AA}$** 

method	basis set	$g$	$c_{IJ}/\text{kHz}$
CCSD(T)	cc-pCVQZ	-1.38	8.47
CCSD(T)	cc-pCV5Z	-1.36	8.52
CCSD(T)	cc-pV5Z	-1.37	8.50
CCSD(T)	cc-pVTZ	-1.18	8.67
CCSDT	cc-pVTZ	-1.19	8.67
CCSD	cc-pVTZ	-1.18	8.71

This value of  $r_0$  corresponds to the minimum of the potential-energy curve at the CCSD(T)/cc-pCV5Z level of theory.

**Extended Data Table 2 | Numerical values of the spin-rotation constant  $c_{IJ}$  and g-factor  $g$  in the vibrational ground state  $v=0$  and in the 15 lowest rotational states  $J$**

$J$	$g$	$c_{IJ}$ (kHz)
0	-1.35	8.27
1	-1.35	8.26
2	-1.35	8.26
3	-1.34	8.26
4	-1.34	8.26
5	-1.34	8.25
6	-1.34	8.25
7	-1.34	8.24
8	-1.33	8.24
9	-1.33	8.23
10	-1.33	8.22
11	-1.32	8.21
12	-1.32	8.20
13	-1.31	8.19
14	-1.31	8.18

**Extended Data Table 3 | Comparison between experiment and theory for spectroscopy of the carrier transitions**

*J* Experiment (kHz) Theory (kHz)

1	10.94(14)	10.73(44)
2	13.55(8)	13.51(80)
3	18.42(10)	18.90(1.27)
4	24.90(15)	25.56(1.75)
5	31.79(7)	32.85(2.20)
6	39.51(5)	40.54(2.64)

Listed are the observed and calculated centre frequencies of the transitions  $|T_J\rangle \leftrightarrow |J, -J - 1/2, -\rangle$ . Experimental uncertainties are statistical, indicating the 68% confidence interval. Theoretical values are computed using the spin-rotation constants and *g*-factors from Extended Data Table 2, a magnetic field  $B = 0.357$  mT, and taking into account off-resonant coupling of the levels  $|T_J\rangle$  and  $|J, -J - 1/2, -\rangle$  to other magnetic sublevels when driven by the Raman beams. Theoretical uncertainties are based on a 5% estimate for the relative uncertainties of the constants, using Gaussian error propagation. Unlike in the case of statistical uncertainties, the theoretical uncertainties might be correlated and hence Gaussian error propagation is only an approximation.